



**HAL**  
open science

# Investigation of Electron Distribution Functions Associated With Whistler Waves at Dipolarization Fronts in the Earth's Magnetotail: MMS Observations

E. Grigorenko, A. Malykhin, D. Shklyar, S. Fadanelli, B. Lavraud, E. Panov,  
L. Avanov, B. Giles, O. Le Contel

► **To cite this version:**

E. Grigorenko, A. Malykhin, D. Shklyar, S. Fadanelli, B. Lavraud, et al.. Investigation of Electron Distribution Functions Associated With Whistler Waves at Dipolarization Fronts in the Earth's Magnetotail: MMS Observations. *Journal of Geophysical Research Space Physics*, 2020, 125 (9), 10.1029/2020JA028268 . hal-03002458

**HAL Id: hal-03002458**

**<https://hal.science/hal-03002458>**

Submitted on 23 Jun 2022

**HAL** is a multi-disciplinary open access archive for the deposit and dissemination of scientific research documents, whether they are published or not. The documents may come from teaching and research institutions in France or abroad, or from public or private research centers.

L'archive ouverte pluridisciplinaire **HAL**, est destinée au dépôt et à la diffusion de documents scientifiques de niveau recherche, publiés ou non, émanant des établissements d'enseignement et de recherche français ou étrangers, des laboratoires publics ou privés.

Copyright

# JGR Space Physics

## RESEARCH ARTICLE

10.1029/2020JA028268

### Key Points:

- Electron distribution function is highly variable on time scales of short narrowband quasi-parallel whistler bursts at and behind DFs
- Electrons with energies 1–5 keV and pitch angles  $\sim 40\text{--}75^\circ$  and  $100\text{--}135^\circ$  make the major contribution to the growth rate of these waves
- The source of the wave bursts is spread out in space and not confined near the neutral plane

### Supporting Information:

- Supporting Information S1

### Correspondence to:

E. E. Grigorenko,  
elenagrigorenko2003@yandex.ru

### Citation:




Grigorenko, E. E., Malykhin, A. Y., Shklyar, D. R., Fadanelli, S., Lavraud, B., Panov, E. V., et al. (2020). Investigation of electron distribution functions associated with whistler waves at dipolarization fronts in the Earth's magnetotail: MMS observations. *Journal of Geophysical Research: Space Physics*, 125, e2020JA028268. <https://doi.org/10.1029/2020JA028268>

Received 23 MAY 2020

Accepted 7 AUG 2020

Accepted article online 25 AUG 2020

## Investigation of Electron Distribution Functions Associated With Whistler Waves at Dipolarization Fronts in the Earth's Magnetotail: MMS Observations

E. E. Grigorenko<sup>1,2,3</sup> , A. Y. Malykhin<sup>1,3</sup> , D. R. Shklyar<sup>1,2</sup> , S. Fadanelli<sup>4</sup> , B. Lavraud<sup>4,5</sup> , E. V. Panov<sup>6</sup> , L. Avanzo<sup>7</sup> , B. Giles<sup>7</sup> , and O. Le Contel<sup>8</sup> 

<sup>1</sup>Space Research Institute of Russian Academy of Science, Moscow, Russia, <sup>2</sup>Department of Space Physics, Moscow Institute of Physics and Technology, Moscow, Russia, <sup>3</sup>Department of Physics of the Earth, St. Petersburg State University, Saint Petersburg, <sup>4</sup>Institut de Recherche en Astrophysique et Planétologie, Université de Toulouse (UPS), Toulouse, France, <sup>5</sup>Laboratoire d'Astrophysique de Bordeaux, Université de Bordeaux, CNRS, Pessac, France, <sup>6</sup>Space Research Institute, Graz, Austria, <sup>7</sup>NASA Goddard Space Flight Center, Greenbelt, MD, USA, <sup>8</sup>Laboratoire de Physique des Plasmas, CNRS, Ecole Polytechnique, Sorbonne Université, Paris, France

**Abstract** Using burst mode Magnetospheric Multiscale (MMS) observations in the plasma sheet (PS), we study the dynamics of electron anisotropy and its relation to quasi-parallel narrowband whistler bursts in 37 dipolarization fronts (DFs) propagating in the Earth's magnetotail along with fast flows at  $-25 R_E \leq X \leq -17 R_E$ . The bursts were observed at the DFs and behind them in the dipolarizing flux bundle (DFB) region with frequencies  $f_{\text{peak}} \sim (0.1\text{--}0.6) f_{ce}$  ( $f_{ce}$  is electron gyrofrequency) and durations approximately a few seconds. The majority of the whistler waves were associated with perpendicular electron temperature anisotropy  $T_{\text{PER}}/T_{\text{PAR}} > 1$ , and the value of this anisotropy decreased by the end of the bursts suggesting electron scattering by the waves. We found that the major contribution to the growth rate of whistler waves is made by resonant electrons with energies  $W_{\text{res}} \sim 1\text{--}5$  keV and pitch angles  $\alpha_{\text{res}} \sim 40\text{--}75^\circ$  and  $\sim 100\text{--}135^\circ$ . In the majority of cases, the largest  $W_{\text{res}}$  was observed at the DF and immediately behind it, while in the DFB the  $W_{\text{res}}$  decreased. The sources of the majority of whistler bursts were not confined near the neutral plane but could be extended into the PS where the perpendicular anisotropy of the local electron distribution provided the positive growth rate of the whistler waves. We show that the observed whistler waves play a significant role in the dynamics of electron velocity distribution in DFs, leading to energy exchange between various parts of electron population and constraining temperature anisotropy of electron distribution.

## 1. Introduction

Dipolarization fronts (DFs) represent the earthward-propagating magnetic structures, which are characterized by a sharp increase in the northward ( $B_z$ ) component of the magnetic field at the spatial scale of the order of ion gyroradius (e.g., Balikhin et al., 2014; Fu et al., 2020; Nakamura et al., 2002; Runov et al., 2009; Sergeev et al., 2009, and references therein). The earthward-propagating DFs are often associated with bursty bulk flows (BBFs) (e.g., Angelopoulos et al., 1992; Merkin et al., 2019; Sitnov et al., 2009; Wiltberger et al., 2015) or with the ballooning/interchange instability (Panov et al., 2019, 2020; Pritchett et al., 2014; Pritchett & Coroniti, 2011) or by “ $B_z$  hump” instability (Birn et al., 2018; Merkin & Sitnov, 2016; Pritchett, 2015; Sitnov et al., 2017). Behind the DF there is a region of enhanced and fluctuating magnetic field and reduced plasma density termed dipolarizing flux bundle (DFB) (e.g., Liu et al., 2013, 2014).

Various types of electron pitch angle distribution (PAD) were reported at and behind DFs. Adiabatic energization of electrons (betatron and/or Fermi) was considered as one of the mechanisms responsible for the electron anisotropy formation. It was suggested that the perpendicular temperature anisotropy ( $T_{\text{PER}}/T_{\text{PAR}} > 1$ ) often observed at and behind the DFs may be due to the betatron acceleration of electrons in a gradually increasing magnetic field (e.g., Birn et al., 2014; Fu et al., 2011; Gabrielse et al., 2016; Khotyaintsev et al., 2011). The parallel anisotropy ( $T_{\text{PER}}/T_{\text{PAR}} < 1$ ) could be caused by Fermi acceleration

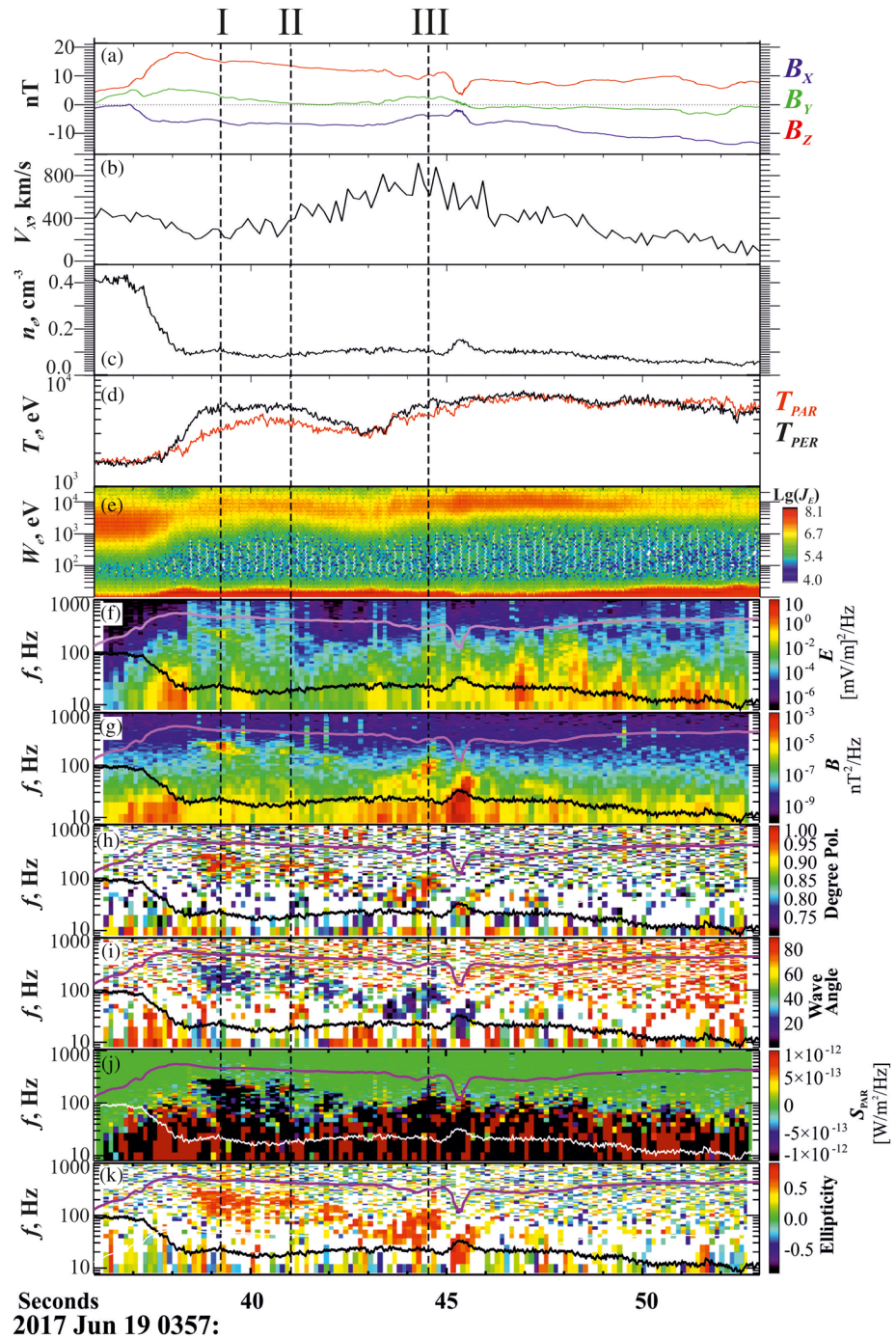


**Figure 1.** An example of a DF observation by MMS-1 on 19 June 2017. From top to bottom are shown three components of the magnetic field (a),  $V_X$  component of ion bulk velocity (b), electron density (c), parallel ( $T_{PAR}$ ) and perpendicular ( $T_{PER}$ ) electron temperatures (d), energy-time (E-T) spectrogram of omnidirectional electron energy flux (e), frequency-time (F-T) spectrograms of the PSD of magnetic field (f) and electric field (g) fluctuations, F-T spectrograms of the polarization degree (h), wave normal angle (i), Poynting flux (j), and ellipticity (k). Vertical dashed lines mark the moments of the maximal amplitude of the PSD of the magnetic field fluctuations observed in bursts (numbered “I–III”) of quasi-parallel narrowband whistler waves. Solid magenta and black/white lines in panels (f)–(k) display the time profiles of the  $f_{ce}$  and  $f_{pp}$ , respectively.

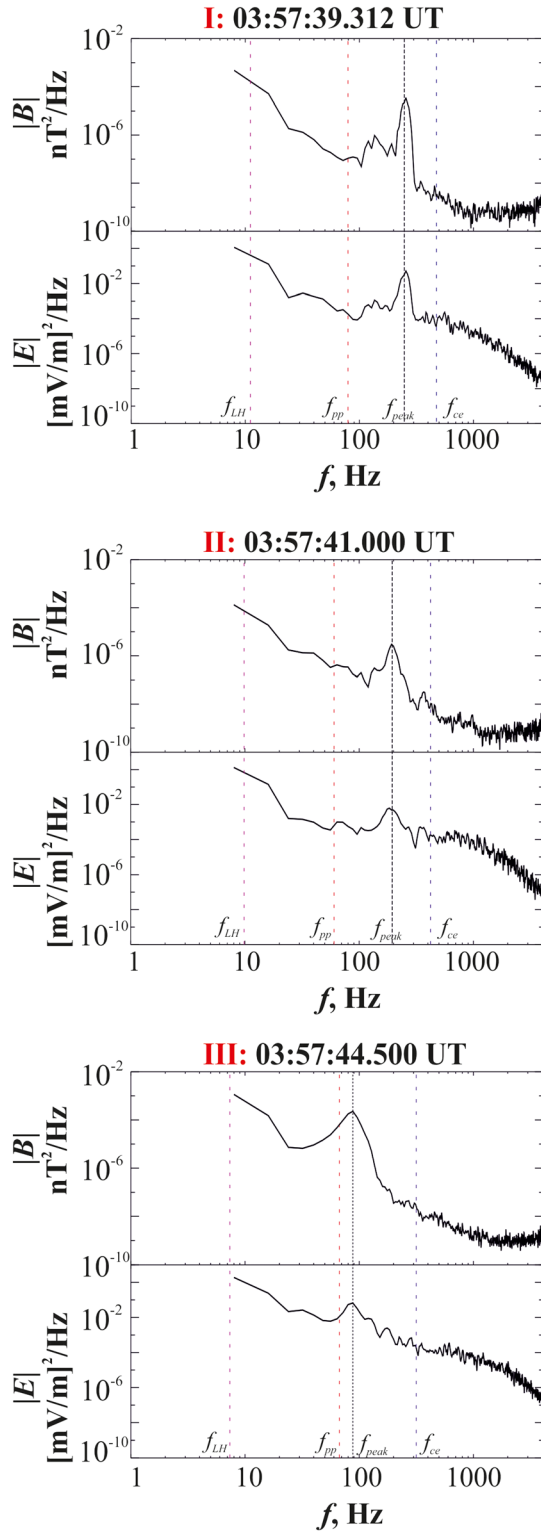


**Figure 2.** The frequency spectra of the PSD of magnetic and electric field fluctuations observed at the Moments “I–III” marked in Figure 1. The characteristic frequencies  $f_{LH}$ ,  $f_{pp}$ ,  $f_{ce}$ , and the frequency of the narrowband quasi-parallel whistler wave,  $f_{peak}$ , are marked by the colored vertical dashed lines in the spectra.

due to the shrinking of the magnetic field lines in the course of DFs propagation toward the Earth (e.g., Fu et al., 2011; Wu et al., 2006).

Besides these types of anisotropy, the “butterfly” distribution consisting of electrons with pitch angles primarily at  $45^\circ$  and  $135^\circ$  and “rolling pin” distribution formed by electrons with pitch angles mainly at  $0^\circ$ ,  $90^\circ$ , and  $180^\circ$  were reported (Liu et al., 2017; Runov et al., 2013; Wu et al., 2013). Both types of distributions were registered behind DFs.

Using Magnetospheric Multiscale (MMS) observations, Zhao et al. (2019) demonstrated that the “rolling pin” distribution appears in the suprathermal energy range: above 1.7 keV. Below 1.7 keV the distribution function of electrons is Maxwellian, while above 1.7 keV it exhibits a power law behavior. C. M. Liu and Fu (2019) using a large amount of DFs observed by Cluster reported that such type of electron distributions with an energy threshold or “anchor point” separating Maxwellian and power law types of distribution is often observed in the DF events with strong whistler waves. Thus, electron interaction with the waves may be related to the formation of such distributions.

The electron temperature anisotropy, in turn, can be a source of various types of waves observed around the DFs including kinetic Alfvén waves and whistler waves (Breuillard et al., 2016; Grigorenko et al., 2016; Le Contel et al., 2009; Viberg et al., 2014; Zhang et al., 2019; Zhang & Angelopoulos, 2014). The generation of whistler waves can be caused by the cyclotron instability excited due to the appearance of electron perpendicular anisotropy  $T_{PER}/T_{PAR} > 1$  (e.g., Gurnett et al., 1976; Khotyaintsev et al., 2011; Sagdeev & Shafranov, 1961; Zhang et al., 1999, 2018). These waves, in turn, may cause the scattering of resonant electrons and the relaxation of anisotropy. The processes of electron anisotropy build up, and its relaxation can modify the electric current system of the DF as well as the local current in the current sheet (CS). In this sense, it is important to define which electron population is mostly affected by a particular type of waves observed around the DFs.

To study the dynamics of the anisotropy of electron velocity distribution and its contribution to the growth rate on the time scale of a whistler burst (approximately several seconds) the high time resolution of 3-D electron distribution observations is required. The Fast Plasma Investigation (FPI) on board MMS probes provides such observations with 30 ms resolution in the burst mode that gives a unique opportunity to investigate this problem.

In this paper, using MMS observations, we have calculated the growth rate of quasi-parallel whistler waves observed in the “growing” DFs events and defined statistically the pitch angle and energy ranges of electrons making the maximum contribution to the growth rate. From our database, we have statistically confirmed that the suprathermal electrons with energies 1–5 keV and pitch angles near  $60^\circ$  and  $120^\circ$  make the major contribution to the growth rate of quasi-parallel whistler waves observed behind the DFs. MMS observations also revealed that a source of whistler waves is likely expanded in space and is not confined within the neutral plane. In

section 2 we present a typical example of the narrowband quasi-parallel whistler wave observations in the DF event and the method of the growth rate calculation. The analysis presented in section 2 has been applied to all DF events from our database in order to obtain the statistical results presented in section 3 and discussed in section 4.

## 2. Observations

We use the burst mode data from the MMS mission (Burch et al., 2016). Observations from FPI (Pollock et al., 2016) in the burst mode provide 3-D electron velocity distribution functions measured in the energy range from  $\sim 10$  eV to 30 keV with 30 ms time resolution, which is sufficient to study the fast variations of electron anisotropy during short whistler bursts. We also use data from fluxgate magnetometer (FGM) (Russell et al., 2016) and search coil magnetometer (SCM) (Le Contel et al., 2016).

We examined the plasma sheet (PS) crossings by MMS at  $-25 R_E \leq X \leq -17 R_E$  and  $|Y_{GSM}| \leq 10 R_E$  for the period from June to September 2017. We selected those DFs intervals in which the spacecraft was located in the inner PS ( $|B_X| \leq 10$  nT), and in which the amplitude of the  $B_Z$  increase was larger than 5 nT. The geocentric solar magnetospheric (GSM) coordinate system is used everywhere in the paper.

### 2.1. Overview of a DF and Associated Whistler Bursts Observed on 19 June 2017 Between 03:57:30 and 03:58:00 UT

On 19 June 2017 between 03:57:37 and 03:58:00 UT MMS spacecraft were located in the PS at  $[-17, -0.5, 1.6] R_E$ . Figure 1 shows an overview of MMS-1 observations for this interval. The observations from the other probes are similar and not shown. A sharp increase in the  $B_Z$  field started at 03:57:36 UT (see Figure 1a) simultaneously with the drop in electron density,  $n_e$  (Figure 1c, this drop may be partly due to missing parallel electrons, which were scattered by whistlers into the loss cone; see Panov et al., 2013, for details) and the increase in electron temperature (Figure 1d). Also, the increase in electron energization is clearly observed in the energy-time spectrogram of omnidirectional electron flux (Figure 1e). The increase in the earthward ion bulk velocity,  $V_X$ , started just after the front (Figure 1b), and the  $V_X$  reached its maximum value  $\sim 800$  km/s behind the DF. All these features indicate that the DF represents a typical earthward-propagating front separating hot and tenuous plasma population from the ambient PS (e.g., Fu et al., 2011; Runov et al., 2011; Schmid et al., 2015; Sergeev et al., 2012).

Just behind the peak of  $B_Z$  field associated with the front, several bursts of whistler waves were observed (Figures 1f and 1g). These waves are characterized by high degree of polarization (close to 1.0, see Figure 1h) and propagation almost antiparallel to the ambient magnetic field (the wave normal angle is less than  $20^\circ$ , and Poynting flux is negative in the frequency range corresponding to the whistler wave, see Figure 1i and 1j, respectively). The waves had the right-hand polarization (the ellipticity was close to 1.0, see Figure 1k). These characteristics of whistler waves are similar to those observed behind the DF by earlier spacecraft missions (e.g., Huang et al., 2012; Le Contel et al., 2009).

The moments of the maximal amplitude of the power spectral density (PSD) of the magnetic field fluctuations observed in each narrowband whistler burst are shown by vertical dashed lines in Figure 1 (Moments “I–III”), and the corresponding frequency spectra are displayed in Figure 2. The bulge in the PSD of the magnetic and electric field fluctuations corresponding to the quasi-parallel whistler waves is located in a finite range of frequencies between proton plasma frequency ( $f_{pp}$ ) and electron gyrofrequency ( $f_{ce}$ ). The peak frequency of these narrowband whistler waves is  $f_{\text{peak}} \sim 0.55f_{ce}$ ,  $0.45f_{ce}$ , and  $0.28f_{ce}$  for the Bursts “I,” “II,” and “III,” respectively.

It is worth noting that whistler emission with the characteristics similar to those discussed above has also been registered at  $\sim 03:57:45$  UT, simultaneously with a local decrease of the ambient magnetic field and a local maximum of plasma density. Such whistler waves associated with magnetic holes were earlier reported in the magnetotail (e.g., Tenerani et al., 2013) and in the magnetosheath (e.g., Yao et al., 2019).

### 2.2. Variations of Electron Anisotropy and Their Relation to the Whistler Bursts

Figure 3 presents the behavior of electron fluxes and anisotropy during the DF event discussed above. The time profile of the  $B_Z$  field is displayed in Figure 3a for reference. The intervals of three bursts of

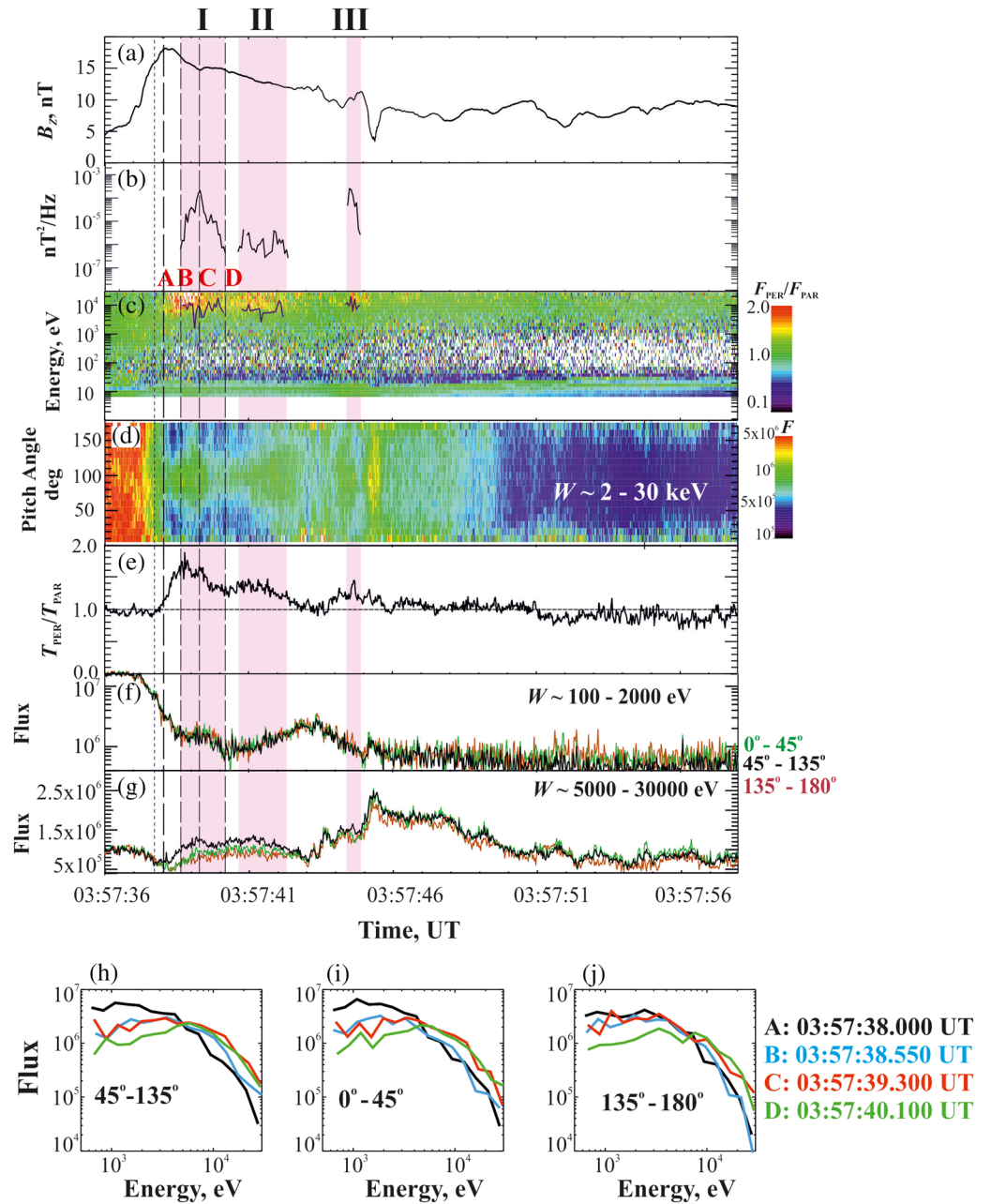


**Figure 3.** From top to bottom: the  $B_z$  field (a), the time profile of the PSD of magnetic field fluctuations corresponding to the frequency of the narrowband whistler waves ( $f_{\text{peak}}$ ) during the intervals of the Bursts “I–III” (shaded by pink) (b), the  $E$ - $T$  spectrogram of the ratio of the flux of electrons with pitch angles close to  $90^\circ$  ( $F_{\text{PER}}$ ) to the flux of electrons moving almost along the magnetic field ( $F_{\text{PAR}}$ ) (c), PAD of electron fluxes for 2–30 keV (d), the time profile of electron temperature anisotropy  $T_{\text{PER}}/T_{\text{PAR}}$  (e), the time profiles of electron fluxes in three pitch angle intervals in the energy range 0.1–2 keV (f), and 5–30 keV (g). Panels (h)–(j) display energy distributions of differential electron fluxes for three pitch angle intervals observed at the Moments “A–D” marked by vertical dashed lines. Solid black lines in panel (c) display the time profiles of the total energy of resonant electrons ( $W_{\text{res}}$ ) contributing to the maximum growth rate of the quasi-parallel whistler waves during the pink shaded Intervals “I–III.”

quasi-parallel narrowband whistler waves are shaded by pink color in the figure, and the time profile of the PSD of magnetic field fluctuations corresponding to the  $f_{\text{peak}}$  in these bursts is shown in Figure 3b.

The electron temperature anisotropy  $T_{\text{PER}}/T_{\text{PAR}}$  started to grow from 1.0 at the DF (this moment is marked by the vertical dotted line) and reached its maximum value  $T_{\text{PER}}/T_{\text{PAR}} \sim 1.9$  behind the  $B_z$  peak

(see Figure 3e). Around this moment, the start of the first whistler burst (I) was registered (see Figure 3b). While the power of magnetic field fluctuations was increasing during the burst, the value of  $T_{PER}/T_{PAR}$  was decreasing. At the moment of the burst power maximum the value of  $T_{PER}/T_{PAR}$  was less than the value observed at the start of the burst. By the end of the first whistler burst  $T_{PER}/T_{PAR}$  decreased to  $\sim 1.3$ . If the observed  $T_{PER}/T_{PAR}$  variation was related to the spatial effect due to the spacecraft crossing, the magnetic tubes connected to the whistler source and containing the anisotropic electrons then the time profiles of the wave power and  $T_{PER}/T_{PAR}$  would be similar. But since  $T_{PER}/T_{PAR}$ , in general, decreased during the burst we suggest that this could be caused by the temporal effect related to electron scattering by the waves. This suggestion is confirmed by the dynamics of electron PAD shown in Figure 3d. The PAD was integrated over the energy range 2–30 keV, which contains the energies of resonant electrons. The PAD demonstrates that each wave burst, including the burst of low-frequency whistler wave associated with the magnetic hole (at  $\sim 03:57:45$  UT, not shown), was preceded by the increase in flux of electrons with pitch angles  $\sim 70$ – $120^\circ$ . By the end of each burst the increase in electron flux expanded in pitch angles indicating the electron scattering by the waves.

Figure 3c presents the color-coded energy-time spectrogram of the ratio of the flux of electrons having pitch angles near  $90^\circ$  ( $F_{PER}$ ) to the flux of electrons moving almost along the magnetic field ( $F_{PAR}$ ). As  $F_{PAR}$  value we used either the flux of electrons moving with pitch angles near  $0^\circ$  or the flux of electrons having the pitch angles near  $180^\circ$  depending on which flux was larger. Figure 3c demonstrates that the increase in  $T_{PER}/T_{PAR}$  value is associated with the increase in  $F_{PER}/F_{PAR}$  up to 2.0 in the higher-energy range ( $\geq 5$  keV). By the end of the first whistler burst the value of  $F_{PER}/F_{PAR}$  decreased in the high-energy range almost to 1.0 along with the decrease in  $T_{PER}/T_{PAR}$ .

A similar behavior of  $T_{PER}/T_{PAR}$  and  $F_{PER}/F_{PAR}$  was observed during the second and third whistler bursts. In every case the increase in  $T_{PER}/T_{PAR}$  was observed simultaneously with the increase in  $F_{PER}/F_{PAR}$  in the high-energy range and they both preceded the start of a given whistler burst. By the end of every whistler burst both  $T_{PER}/T_{PAR}$  and  $F_{PER}/F_{PAR}$  decreased.

Figures 3f and 3g show time profiles of electron fluxes in three pitch angle intervals integrated over 100–2,000 and 5,000–30,000 eV energy ranges, respectively. During the time of whistler bursts there is a clear tendency for lower- and higher-energy fluxes to vary in antiphase, which may imply energy exchange between two particle populations via whistler waves. This suggestion is consistent with the dynamics of electron differential fluxes during the Whistler Burst “I” presented in Figures 3h–3j. Each panel shows the electron flux, integrated over certain pitch angle interval, as a function of energy, at four successive moments of Time “A–D” before, during, and at the end of the wave burst (these moments are marked by vertical dashed lines in Figure 3). There is a tendency for lower-energy fluxes ( $< 5$  keV) to decrease with time, that is, to be larger before wave events and smaller after, while for higher-energy electrons ( $\geq 5$  keV) the tendency is opposite. Such a behavior of electron fluxes is observed in all three pitch angle intervals. A similar dynamics was detected in electron fluxes during the other wave bursts (not shown).

The increase in the electron perpendicular anisotropy observed in the high-energy range just before the start of the whistler bursts, and the subsequent relaxation of this anisotropy by the end of the burst suggest that the anisotropy of electron velocity distribution could cause the whistler burst generation, and the subsequent wave-particle interactions aimed at isotropizing the electron distribution function. Thus, the changes in electron velocity distribution function observed in the energy range  $\geq 1$  keV during the whistler bursts can be caused by energy exchange between lower- and higher-energy electrons via their interaction with the whistler waves and by the scattering of resonant electrons which decreased the perpendicular anisotropy by the end of each burst.

To check this assumption, in the next subsection we calculate the growth rate ( $\gamma$ ) of the quasi-parallel whistler waves from the observed 3-D electron velocity distribution function and define the energy and pitch angle ranges of the resonant electrons which make maximum contribution to the growth rate  $\gamma$ .

### 2.3. The Analysis of $\gamma$ and Definition of the Characteristics of Resonant Electrons

MMS observations in the burst mode allow us to study the dynamics of  $\gamma$  and to determine the characteristics (energies and pitch angles) of the resonant electrons with the unprecedented time resolution during a short (approximately a few seconds) whistler burst.

From general expression for resonance velocity corresponding to the  $n$ th cyclotron resonance:

$$V_{res_n} = \frac{\omega - n\omega_{ce}}{k_{\parallel}}$$

it follows that for wave frequency  $\omega \sim \omega_{ce}/2$ ,  $|V_{res_0}| \sim |V_{res_{-1}}|$ , and  $|V_{res_{-1}}| \sim 3|V_{res_{-2}}|$ . This

by no means implies that these resonances are equally important. The point is that the fulfillment of resonance conditions is only necessary but not sufficient condition for a resonance to play a role, which also requires that the amplitude of wave-particle interaction is significant. For parallel propagating whistlers, the amplitudes of interaction with electrons at all cyclotron resonances, but  $n = 1$ , are equal to 0, and for waves propagating at small angles to the ambient magnetic field these amplitudes are small (see, e.g., Shklyar & Matsumoto, 2009). That is why, at finite, but small, angles of propagation, the first cyclotron resonance  $n = 1$  remains the most important. Thus, the parallel energy of resonant electrons ( $W_{\parallel res}$ ) can be calculated by using the well-known dispersion relation for quasi-parallel whistler waves, which gives

$$W_{\parallel res} = m_e c^2 \frac{(f_{ce} - f_{peak})^3}{2f_{peak} f_{pe}^2},$$

where  $m_e$  is the electron mass,  $c$  is the speed of light,  $f_{ce}$  and  $f_{pe}$  are electron gyrofrequency and plasma frequency, respectively, and  $f_{peak}$  is the frequency of the narrowband whistler wave (see Figure 2). By using the local measurements of  $f_{ce}$ ,  $f_{pe}$ , and  $f_{peak}$ , we calculated the  $W_{\parallel res}$  for each time moment during each interval of the whistler bursts shaded in pink in Figure 3. We found that the  $W_{\parallel res}$  ranged from  $\sim 900$  eV to  $\sim 6$  keV during the whistler bursts. This means that the total energy of electrons that can contribute to the positive  $\gamma$  and efficiently interact with the whistler waves should be larger than  $W_{\parallel res}$ . To define the ranges of total energy,  $W_{res}$ , and pitch angles of the resonant electrons,  $\alpha_{res}$ , we calculate  $\gamma(f, t)$  during each interval of whistler bursts. Before presenting the results of numerical calculation of the  $\gamma$ , we briefly discuss the analytical formulas used.

General expression for linear growth rate  $\gamma$  of parallel propagating whistler mode wave has been obtained by Sagdeev and Shafranov (1961) and may also be found in various publications (see, e.g., the monograph by Trakhtengerts & Rycroft, 2008). Keeping in mind that the experimentally measured differential electron fluxes depend on particle kinetic energy  $W$  and pitch angle  $\alpha$ , we will assume that electron distribution function  $F_0$  is expressed in terms of  $W$ , the quantity  $s = \sin^2 \alpha$ , that is the sine squared of particle pitch angle, and the sign of its parallel velocity, that is, sign ( $\cos \alpha$ ).

We should underline that, no matter in which variables the distribution function is expressed, it is always normalized in such a way that its integral over velocity space gives particle density:  $\int F_0 d^3v = n(r)$ . In the variables specified above the expression for  $\gamma$  has the form:

$$\gamma = \frac{\pi^2 c^5 e^2 (f_{ce} - f)^{17/2}}{f_{ce} f_{pe}^3 f_{pe}^7} \int_0^1 F'_0(s) \frac{s ds}{(1-s)^3}. \quad (1)$$

Here  $e$  is the electron charge,  $f$  is the wave frequency for which the growth rate is calculated, and the quantity  $F'_0(s)$  is expressed through derivatives of the distribution function with respect to  $W$  and  $s$  as follows:

$$F'_0(s) = \left[ \frac{\partial F_0}{\partial W} + \frac{1}{W} \left( \frac{f_{ce}}{f} - s \right) \frac{\partial F_0}{\partial s} \right]_{W = W_{\parallel res}/(1-s)} \quad (2)$$

where  $W_{\parallel res}$  is defined above. Since, after taking derivatives, the value of kinetic energy is equated to  $W_{\parallel res}/(1-s)$ , the quantity  $F'_0$  becomes independent of particle energy  $W$ .

Expression for the growth rate (1) takes into account solely the first cyclotron resonance  $n = 1$ , the only one which exists for strictly parallel wave propagation and the one which is the most important at small angles of propagation (see, e.g., Shklyar & Matsumoto, 2009).

One should keep in mind that, besides  $s$ ,  $f$ ,  $f_{ce}$ , and  $f_{pe}$ , the quantity  $F'_0$  depends also on the sign of particle parallel velocity, as the distribution function  $F_0$  does. Since particles moving in different directions with



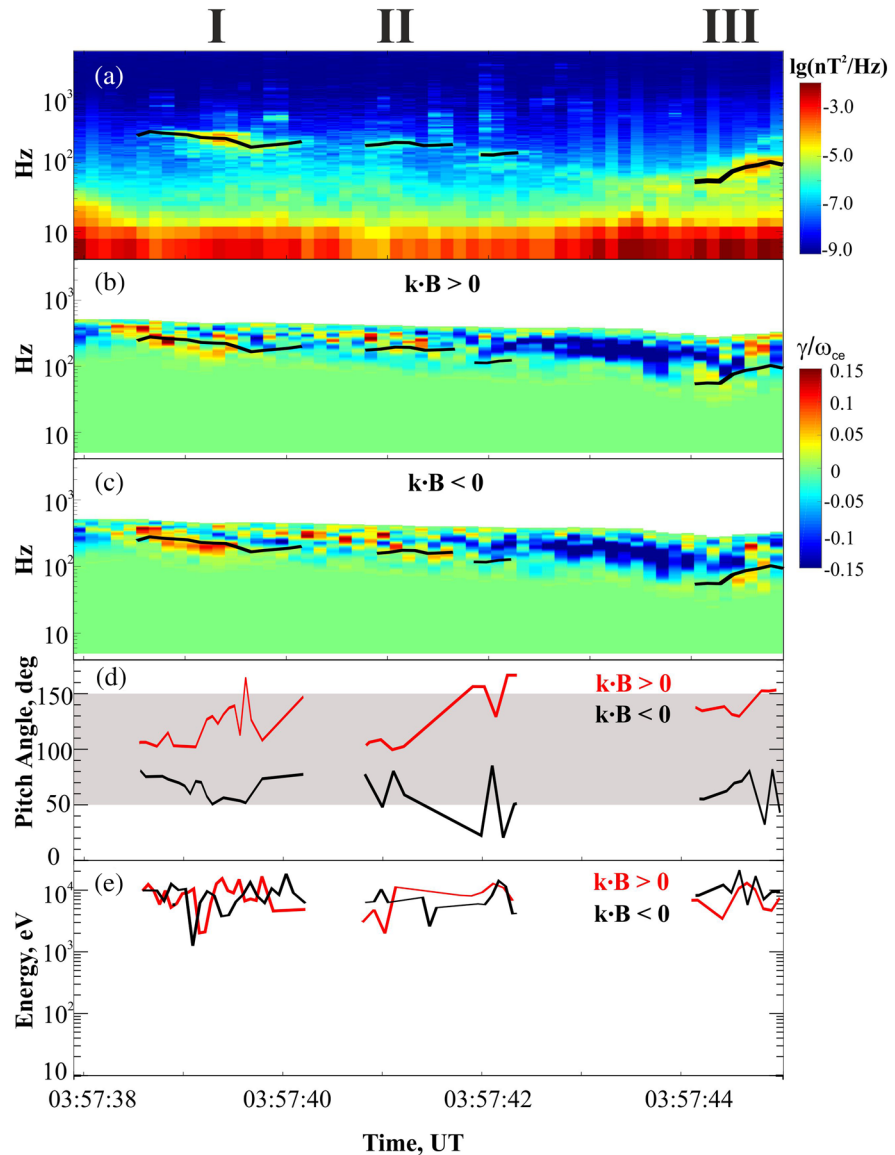


**Figure 4.** From top to bottom:  $F$ - $T$  spectrogram of the PSD of the magnetic field fluctuations (a);  $F$ - $T$  distribution of the normalized growth rate values ( $\gamma/\omega_{ce}$ ) calculated for the whistler wave propagating parallel ( $\mathbf{k}\cdot\mathbf{B} > 0$ ) (b) and antiparallel ( $\mathbf{k}\cdot\mathbf{B} < 0$ ) (c) to the ambient magnetic field  $\mathbf{B}$ ; the time profiles of the pitch angles of electrons contributing to the maximum of  $\gamma$  for the waves with  $\mathbf{k}\cdot\mathbf{B} > 0$  (shown by red) and for the waves with  $\mathbf{k}\cdot\mathbf{B} < 0$  (shown by black) (d); the time profiles of the total energy of electrons contributing to the maximum of  $\gamma$  for the waves with  $\mathbf{k}\cdot\mathbf{B} > 0$  (shown by red) and for the waves with  $\mathbf{k}\cdot\mathbf{B} < 0$  (shown by black) (e). Solid black lines in panels (a)–(c) display the time profiles of  $f_{\text{peak}}$ .

respect to the ambient magnetic field amplify waves propagating in different directions, the growth rates of these waves may depend not only on their frequency but also on the direction of propagation, on conditions that the distribution function really depends on sign ( $\cos \alpha$ ).

Expression 1 permits to calculate the growth rate from experimental data on particle fluxes, without any assumptions about the form of the distribution function. This expression, however, is written in CGS system of units, while the measured differential flux  $J$  is usually expressed in practical units  $1/(\text{cm}^2 \cdot \text{s} \cdot \text{ster} \cdot \text{keV})$ . The distribution function  $F_0$  in CGS units is connected with  $J$  by the relation (Cornilleau-Wehrin et al., 1985; Shklyar et al., 2020):

$$F_0 = 1.67 \cdot 10^{-37} \frac{J}{W_{keV}} \quad (3)$$

where  $J$  is the differential particle flux in practical units indicated above and  $W_{keV}$  is particle energy in keV. As a matter of fact, MMS measurements provide differential energy flux  $J_E$  in keV/(cm<sup>2</sup> · s · ster · keV) from which the differential particle flux  $J$  in each energy channel is obtained by dividing the energy flux by the average energy in this channel.

Before proceeding to the results of growth rate calculations, one important remark is in order. Expressions 1 and 2 were originally obtained for linear growth rate in a homogeneous plasma. However, as has been shown in a number of works (e.g., Shklyar & Matsumoto, 2009, and references therein), in an inhomogeneous plasma and in the absence of phase trapped particles, the expression for nonlinear growth rate is very close to (1), assuming local distribution function and plasma parameters. At the same time, as is well known, quasilinear theory adopts the linear expression for the wave growth rate calculated with the help of phase-averaged, slowly varying in time distribution function, so the experimentally measured distribution function that we use is exactly this one. Thus, our consideration is valid in a wide range of cases, excepting the case of weak inhomogeneity for quasi-monochromatic wave, which hardly takes place at DFs. We should also mention that Expression 1 is obtained under condition  $\gamma/2\pi f \ll 1$ , while if a strong inequality is violated, it should only be considered as a credible estimation.

In Figures 4b and 4c we present the color-coded frequency-time distribution of the growth rate value ( $\gamma/\omega_{ce}$ ) normalized to the local electron gyrofrequency  $\omega_{ce} = 2\pi \cdot f_{ce}$  calculated for the whistler wave propagating parallel ( $\mathbf{k} \cdot \mathbf{B} > 0$ ) and antiparallel ( $\mathbf{k} \cdot \mathbf{B} < 0$ ) to the ambient magnetic field  $\mathbf{B}$ , respectively. To calculate the growth rate, we averaged 3-D electron velocity distribution functions over 120 ms in order to avoid zero values casually appearing in some angular and energy channels and resulting in very large gradients of the distribution function in phase space (see (1)). Figure 4a shows the color-coded frequency-time spectrogram of the PSD of the magnetic field fluctuations for reference. The time profile of the observed frequency of narrowband whistler waves  $f_{peak}$  is displayed by the black solid line in Figures 4a–4c.

The frequency-time distributions of  $\gamma/\omega_{ce}$  are slightly different for the whistler waves propagating parallel and antiparallel to  $\mathbf{B}$ . This means that there is some asymmetry in the electron velocity distribution function with respect to the pitch angle  $\alpha = 90^\circ$ .

During the Bursts I and II there is a good agreement between the observed  $f_{peak}$  and the frequency at which the maximum value of  $\gamma/\omega_{ce}$  is observed ( $f_\gamma$ ). This indicates the spacecraft proximity to the source of whistler waves. For the Burst III the agreement between  $f_{peak}$  and  $f_\gamma$  becomes worse but  $\gamma/\omega_{ce}$  is still positive near the  $f_{peak}$ . Thus, we may suggest that the anisotropy of the local electron velocity distribution can be responsible for the whistler wave generation at least for the Bursts “I” and “II.” Comparing Figures 4b and 4c, we can see that the best agreement between  $f_{peak}$  and  $f_\gamma$  is observed for the waves with  $\mathbf{k} \cdot \mathbf{B} < 0$ . This is in agreement with the direction of Poynting flux measured during these bursts (see Figure 1j).

To define the local characteristics of electron population that could be responsible for the wave generation and/or efficiently interact with the propagating whistler wave, we calculated the pitch angles  $\alpha_{res}$  and the total energies  $W_{res} = W_{||res}/\cos^2\alpha_{res}$ , which make the main contribution to the maximal  $\gamma$  at each moment of time within each burst. The results are presented in Figures 4d and 4e as the time profiles of the  $\alpha_{res}$  and  $W_{res}$ , respectively. The red profiles are calculated for the whistler waves propagating parallel to  $\mathbf{B}$  and the black profiles are calculated for the waves propagating antiparallel to  $\mathbf{B}$ .

At the start of Bursts “I” and “II” the maximum contribution to the most unstable wave comes from electrons with  $\alpha_{res}$  close to  $\sim 80^\circ$  and  $\sim 100^\circ$  for the waves with  $\mathbf{k} \cdot \mathbf{B} < 0$  and  $\mathbf{k} \cdot \mathbf{B} > 0$ , respectively. At the start of Burst “III” the maximum contribution is made by electrons with  $\alpha_{res} \sim 50^\circ$  and  $\sim 140^\circ$  for the waves with  $\mathbf{k} \cdot \mathbf{B} < 0$  and  $\mathbf{k} \cdot \mathbf{B} > 0$ , respectively. During the whistler bursts  $\alpha_{res}$  varies mainly in the range  $\sim 50$ – $150^\circ$  (this interval of pitch angles is grayed out in Figure 4d). Overall, this result is in line with the assumption that the perpendicular anisotropy of electron velocity distribution makes the main contribution to the maximum  $\gamma$ .

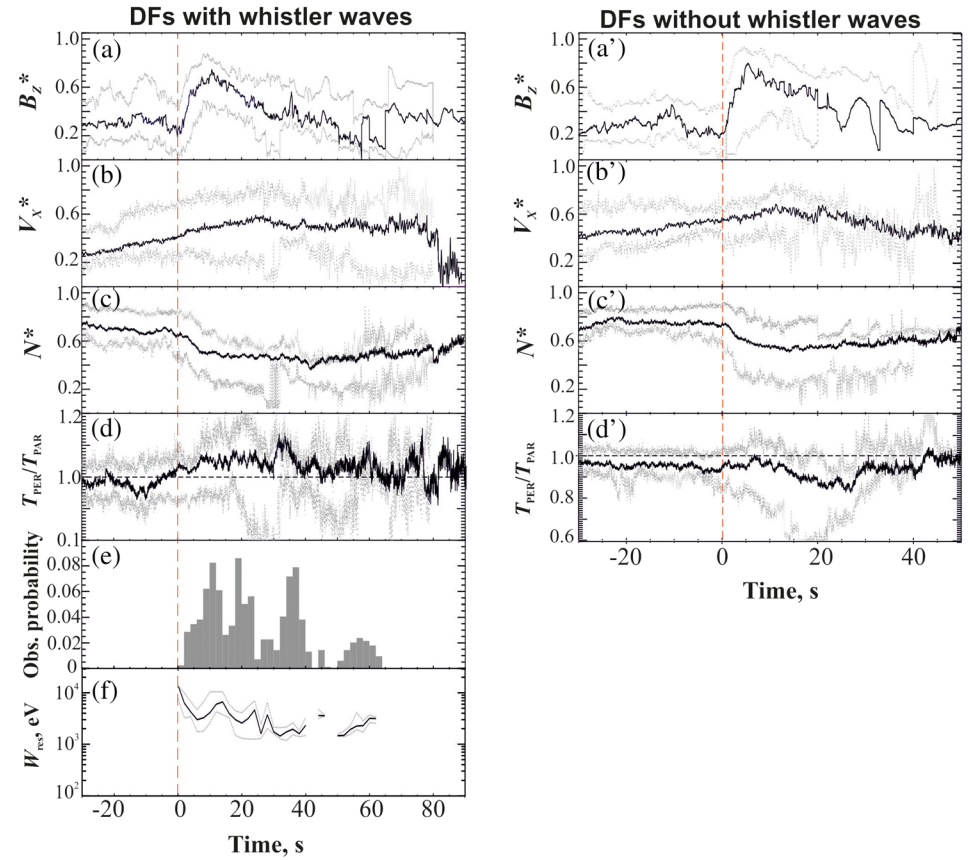


**Figure 5.** (a–f) The epoch analysis of the DF events with whistler waves. From top to bottom: the epoch profiles of the median values of the normalized  $B_Z^*$  (a), ion  $V_X^*$  (b), electron density  $N^*$  (c),  $T_{PER}/T_{PAR}$  (d), the statistical distribution of probability to observe the narrowband quasi-parallel whistler waves versus the epoch time (e), and the epoch profile of the median value of  $W_{res}$  (f). (a'–d') The similar analysis of the DF events without quasi-parallel whistler waves. The gray dotted lines show the lower and upper quartiles. Vertical red dashed line marks the zero epoch time corresponding to the start of the DFs.

The total energy of the resonant electrons  $W_{res}$  is also highly variable and ranges between 2 and 20 keV for all whistler bursts. We have plotted  $W_{res}(t)$  profile onto the energy-time color-coded distribution of  $F_{PER}/F_{PAR}$  shown in Figure 3c by black solid line (for  $\mathbf{k} \cdot \mathbf{B} < 0$ ). It is seen that the  $W_{res}(t)$  marks the low-energy boundary of the energy range at which the largest  $F_{PER}/F_{PAR}$  values were observed during the whistler bursts. Thus, thermal and suprathermal electron populations should interact efficiently with the observed whistler bursts that causes the variation of electron velocity distribution function in this energy range.

### 3. Statistical Results

We have analyzed burst mode MMS observations in the PS at  $-25 R_E \leq X \leq -17 R_E$  and  $|Y_{GSM}| \leq 10 R_E$  from June to September 2017. We selected the DF events in which the spacecraft was located in the inner PS ( $|B_X| \leq 10$  nT) and in which a sharp increase in the  $B_Z$  field with amplitude larger than 5 nT was observed within a time window  $< 3$  s. Finally, we collected 66 isolated DFs propagating earthward. The list of events is presented in the supporting information. In 37 DF events the bursts of quasi-parallel narrowband whistler waves similar to that presented in Figures 2 and 3 were detected.

To identify a quasi-parallel narrowband whistler wave, we analyze the frequency spectra of the magnetic field fluctuations ( $\delta B$ ) measured by the SCM at each time moment within a given DF event and search for the presence of a local maximum or bulge in the frequency range between the lower hybrid frequency ( $f_{LH}$ ) and electron gyrofrequency ( $f_{ce}$ ) since whistler waves are usually observed in this frequency range

(e.g., Liang et al., 2012). We find the local maximum  $\delta B_{\text{peak}}(f_{\text{peak}})$  in the observed spectrum by using the gradient descent method (e.g., Akilov & Kantorovich, 1982), and, if the amplitude of this maximum  $\delta B_{\text{peak}}$  is at least 10 times larger than the value of  $\delta B(f_0)$  (where  $f_0$  is the left boundary of frequency range at which  $\Delta(\delta B)/\Delta f > 0$  is observed), we identify this local maximum in the spectrum as the signature of the narrowband whistler wave with the frequency  $f = f_{\text{peak}}$ . Then, to be sure that this narrowband fluctuations represent the quasi-parallel whistler wave, we check the value of wave normal angle and ellipticity at  $f = f_{\text{peak}}$  to be less than  $40^\circ$  and larger than 0.6, respectively.

We identified 158 bursts of narrowband quasi-parallel whistler waves in 37 DF events from our database. In the other DFs (29 events) the quasi-parallel whistler waves were not observed. In this paper we do not consider the oblique whistler waves for which the angle between the wave vector  $\mathbf{k}$  and the ambient magnetic field  $\mathbf{B}$  is larger than  $40^\circ$ .

In order to reveal statistically where within the DF the quasi-parallel narrowband whistler waves are more frequently observed, we apply a superposed epoch analysis to those DF events in which the whistler waves were detected. The epoch analysis was applied to the following parameters:  $B_Z$  field, the  $X$  component of ion bulk velocity ( $V_X$ ), electron density ( $N_e$ ), and  $T_{\text{PER}}/T_{\text{PAR}}$ . For each event, the  $B_Z$ ,  $V_X$  and  $N_e$  were normalized to the corresponding maximum values observed in each event:  $B_Z^*(t) = B_Z(t)/B_{Z,\text{max}}$ ;  $N_e^* = N_e(t)/N_{e,\text{max}}$ ;  $V_X^* = V_X(t)/V_{X,\text{max}}$ . As the epoch time ( $t_0 = 0$ ) we use the DF start for each event similarly to the previous study by, for example, Fu et al. (2012).

Figures 5a–5d show the epoch profiles of the aforementioned parameters for the DFs with whistler waves. The events from our database possess features typical of the earthward-propagating DFs: The ion bulk velocity increases behind the DF, plasma density decreases, and temperature increases (not shown) (e.g., Runov et al., 2011). In the DFs the increase in the magnetic field causes the betatron energization of electrons and the increase in  $T_{\text{PER}}$ . This is actually observed at the  $T_{\text{PER}}/T_{\text{PAR}}$  epoch profile: before the DF onset the  $T_{\text{PER}}/T_{\text{PAR}}$  experiences variation around 1.0, while at the onset and in the DFB region behind the DF the  $T_{\text{PER}}/T_{\text{PAR}}$  becomes  $>1.0$  (see Figure 5d). In Figure 5e we present the statistical distribution of probability to observe the narrowband quasi-parallel whistler waves versus the epoch time in each event from our database. The distribution has the local maximums both near the  $B_Z^*$  peak and in the DFB where the  $T_{\text{PER}}/T_{\text{PAR}} > 1.0$ .

In Figures 5a'–5d' we show the epoch profiles of  $B_Z^*$ ,  $N_e^*$ ,  $V_X^*$  and  $T_{\text{PER}}/T_{\text{PAR}}$  for the DF events without quasi-parallel whistler waves. The  $N_e^*(t)$  and  $V_X^*(t)$  experience a similar behavior around the DFs with and without the quasi-parallel whistler waves. However, the median value of  $T_{\text{PER}}/T_{\text{PAR}}$  (see Figure 5d') is  $\leq 1$  both at and behind the DFs. Also, the statistical analysis of electron temperature anisotropy presented in Figure 6f showed that in these DF events the value of  $T_{\text{PER}}/T_{\text{PAR}}$  was either close to 1.0 or less than 1.0. Thus, we may suggest that the presence of perpendicular temperature anisotropy is an important factor for quasi-parallel whistler wave generation. Viberg et al. (2014) also reported that whistlers are most often detected in DFB following the DF in association with anisotropic electron distributions ( $T_{\text{PER}} > T_{\text{PAR}}$ ), which could be formed by betatron electron energization at the DFs.

Figure 6 displays the main characteristics of the narrowband whistler bursts from our database. The majority of waves have the  $f_{\text{peak}} \sim (0.1-0.6)f_{\text{ce}}$  (see Figure 6a) and durations less than 5 s (Figure 6b). For these waves, the propagation angle with respect to the ambient magnetic field is less than  $35^\circ$  (see Figure 6c) and the ellipticity ranged from 0.6 to 0.8; that is, the waves have right-hand polarization (Figure 6d). Using the dispersion relation for quasi-parallel whistler waves, the observed wave frequency, and local plasma parameters, we calculated the wave length,  $\lambda$ , and found that for the majority of waves  $\lambda \sim (1-2)\lambda_e$  ( $\lambda_e$  is electron inertia length) (see Figure 6e). In Figure 6f we display the distribution of probability to observe a given value of electron anisotropy  $T_{\text{PER}}/T_{\text{PAR}}$  at the start of each whistler burst from our database. About 70% of the whistler waves were associated with the perpendicular electron anisotropy  $T_{\text{PER}}/T_{\text{PAR}} > 1.1$ . In the bottom of Figure 6f we present the distribution of probability to observe a given value of  $T_{\text{PER}}/T_{\text{PAR}}$  at each time moment within those DF events from our database in which the quasi-parallel whistler waves were not detected. This distribution maximizes at  $T_{\text{PER}}/T_{\text{PAR}} \leq 1.1$  and in  $\sim 65\%$  of such DF events the parallel electron anisotropy  $T_{\text{PER}}/T_{\text{PAR}} < 1.0$  was observed. Thus, we may suggest that the quasi-parallel narrowband whistler waves are mainly associated with a rather strong perpendicular electron anisotropy.

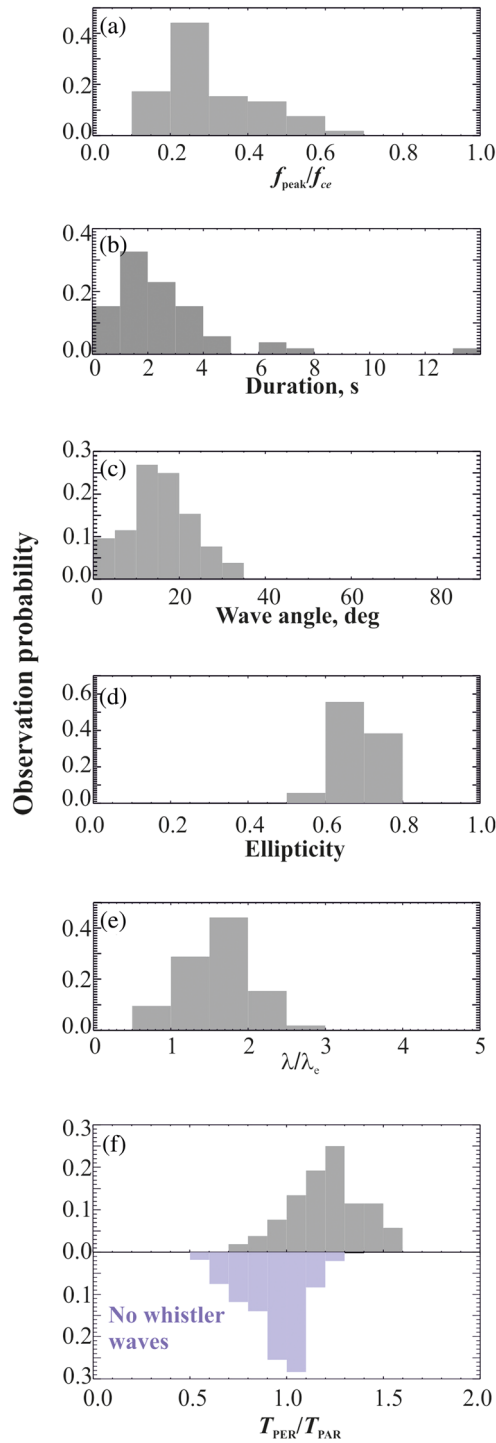


**Figure 6.** The distributions of probability to observe the following characteristics of the narrowband whistler bursts from our database: the observed frequency of waves,  $f_{\text{peak}}$ , normalized to the local  $f_{\text{ce}}$  (a), the whistler burst durations (b), the wave angle (c), the ellipticity (d), the wavelength  $\lambda$  normalized to the local electron inertia length,  $\lambda_e$  (e), and the electron temperature anisotropy  $T_{\text{PER}}/T_{\text{PAR}}$  observed at the start of whistler bursts (gray shaded histogram) and the  $T_{\text{PER}}/T_{\text{PAR}}$  observed during those DF events in which quasi-parallel whistler waves were not observed (lilac histogram) (f).

To statistically define the typical values of total energy ( $W_{\text{res}}$ ) and pitch angles ( $\alpha_{\text{res}}$ ) of electrons making the contribution to the growth rate of narrowband quasi-parallel whistler waves, we calculate  $W_{\text{res}}$  and  $\alpha_{\text{res}}$  at each time moment during each burst from our database by determining pitch angles  $\alpha_{\text{res}}$  and the corresponding values of  $W_{\text{res}} = W_{\text{Ires}}/\cos^2\alpha_{\text{res}}$ , which make the main contribution to the integral in (1). Figure 7 shows the statistical distributions of  $W_{\text{res}}$  (the top panel) and  $\alpha_{\text{res}}$  (the middle panel) of electrons making maximum contribution to the growth rate of the waves propagating parallel ( $\mathbf{k}\cdot\mathbf{B} > 0$ , pink-shaded histograms) and antiparallel ( $\mathbf{k}\cdot\mathbf{B} < 0$ , gray-shaded histograms) to the ambient magnetic field. In the majority of cases  $W_{\text{res}} \sim 1\text{--}5$  keV both for the waves propagating parallel and antiparallel to  $\mathbf{B}$ . The PADs show that in the majority of cases electrons with  $\alpha_{\text{res}} \sim 100\text{--}135^\circ$  make maximum contribution to the growth rate of the waves with  $\mathbf{k}\cdot\mathbf{B} > 0$ , while electrons with  $\alpha_{\text{res}} \sim 40\text{--}75^\circ$  contribute to the growth rate of the whistler waves with  $\mathbf{k}\cdot\mathbf{B} < 0$ . Thus, suprathermal electrons with pitch angles rather close to  $\sim 60^\circ$  and  $\sim 120^\circ$  and moving in the opposite direction to the waves efficiently interact with the quasi-parallel whistler waves. Electrons with  $\alpha_{\text{res}}$  close to  $0^\circ$  or  $180^\circ$  do not contribute to the growth rate of quasi-parallel whistler waves. We would like to stress that, when we speak about electrons making the main contribution to the growth rate, we always mean the frequency that corresponds to maximum growth rate, that is, the frequency of the most unstable wave.

The bottom panel in Figure 7 displays the distribution of probability to observe a given value of the difference between the observed frequency of the narrowband quasi-parallel whistler waves ( $f_{\text{peak}}$ ) and the frequency corresponding to the value of maximum growth rate ( $f_{\gamma}$ ) calculated from the local electron velocity distribution function measured within each wave burst from our database. At most points in time the value  $|f_{\text{peak}} - f_{\gamma}|/f_{\text{peak}}$  is found to be less than 0.5. This may indicate that at such time the local electron velocity distribution is responsible for the wave generation; that is, the wave source is located close to the spacecraft.

#### 4. Discussion

In this paper, using the advantage of MMS observations, we have studied the dynamics of electron anisotropy associated with short bursts of quasi-parallel narrowband whistler waves observed in DF events. The DF events from our database represent isolated fronts propagating in the Earth's magnetotail embedded in the high-velocity bulk flows at  $-25 R_E \leq X \leq -17 R_E$ . Since in these events the  $V_X$  velocity of bulk flow increases behind the front, they can be classified as the “growing” DFs (e.g., Fu et al., 2011). Below we summarize the main features of whistler bursts observed during such events.

1. The narrowband quasi-parallel whistler wave is observed as a bulge in frequency spectra of the PSD of the magnetic field fluctuations. The frequency of these waves  $f_{\text{peak}} \sim (0.1\text{--}0.6)f_{\text{ce}}$ . The majority of these bursts have durations  $< 5$  s (see Figures 6a and 6b).
2. During the DF events from our database the whistler waves were more frequently observed near the maximum of the  $B_Z$  field as well as in the DFB behind the DF (see Figure 5e).

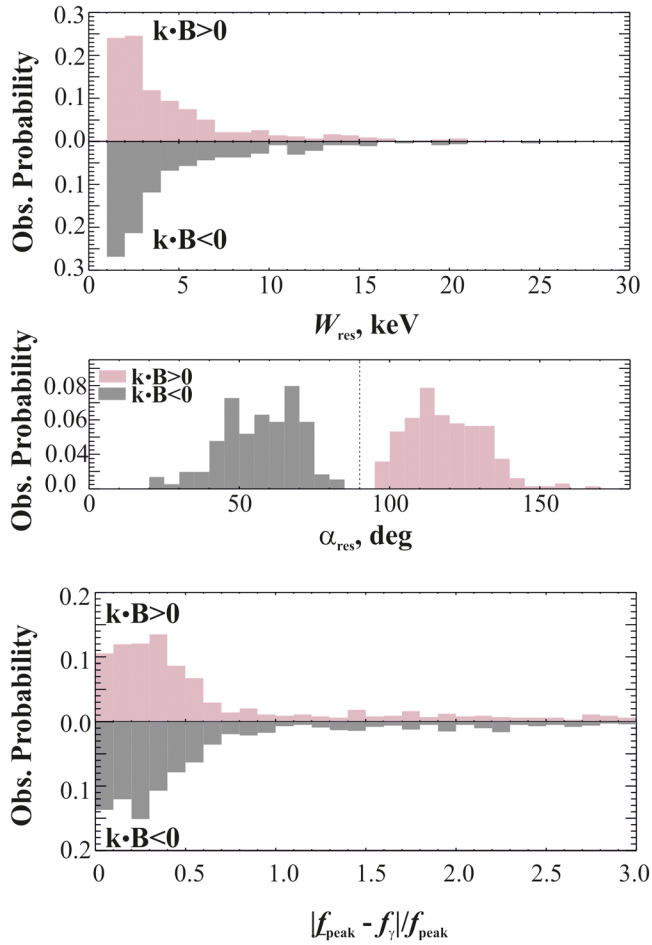


**Figure 7.** The statistical distributions of  $W_{\text{res}}$  (the top panel) and  $\alpha_{\text{res}}$  (the middle panel) of electrons contributing to the maximum growth rate of the waves propagating parallel ( $\mathbf{k} \cdot \mathbf{B} > 0$ , pink-shaded histograms) and antiparallel ( $\mathbf{k} \cdot \mathbf{B} < 0$ , gray-shaded histograms) to the ambient magnetic field. The bottom panel displays the distribution of probability to observe a given value  $|f_{\text{peak}} - f_{\gamma}|/f_{\text{peak}}$  for the waves with  $\mathbf{k} \cdot \mathbf{B} < 0$  (gray-shaded histograms) and  $\mathbf{k} \cdot \mathbf{B} > 0$  (pink-shaded histograms).

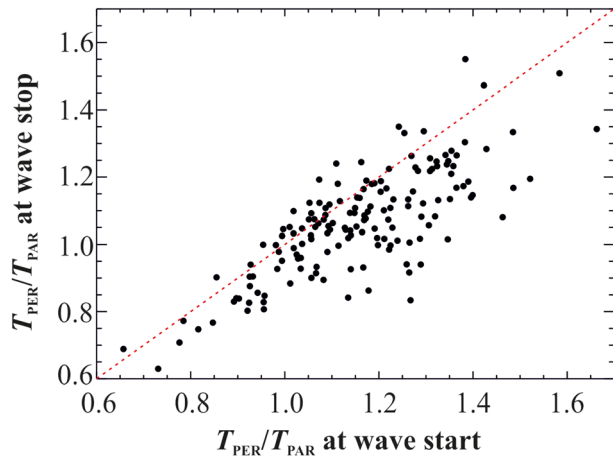


**Figure 8.** A scatterplot of the  $T_{\text{PER}}/T_{\text{PAR}}$  value observed at the start of each whistler burst versus the corresponding value observed at the end of the burst.

3. In the majority of wave bursts from our data, the angle between the wave vector  $\mathbf{k}$  and the ambient magnetic field  $\mathbf{B}$  was  $\sim 10\text{--}20^\circ$ , and ellipticity was 0.6–0.8 (see Figures 6c and 6d).
4. The whistler waves had wavelengths between  $0.5\lambda_e$  and  $2.5\lambda_e$  (where  $\lambda_e$  is electron inertial length) (see Figure 6e).
5. The majority of whistler waves were associated with the electron temperature anisotropy  $T_{\text{PER}}/T_{\text{PAR}} > 1.0$  (see Figure 5d and the top histogram in Figure 6f).
6. Electrons with pitch angles  $\alpha_{\text{res}} \sim 100\text{--}140^\circ$  and  $\alpha_{\text{res}} \sim 40\text{--}80^\circ$  made maximum contribution to the growth rate of whistler waves propagating quasi-parallel ( $\mathbf{k} \cdot \mathbf{B} > 0$ ) and antiparallel ( $\mathbf{k} \cdot \mathbf{B} < 0$ ) to  $\mathbf{B}$ , respectively. Electrons with  $\alpha_{\text{res}}$  close to  $0^\circ$  or  $180^\circ$  do not contribute to the growth rate of quasi-parallel whistler waves.
7. For the majority of events from our database, the total energy of electrons contributing to the growth rate was between  $\sim 1$  and 5 keV (Figure 7).

Narrowband quasi-parallel whistler waves were observed in  $\sim 56\%$  of the DF events from our database. In the other DF events either no whistler waves or oblique waves were detected.

In Figure 8 we present a scatterplot of the  $T_{\text{PER}}/T_{\text{PAR}}$  value observed at the start of each whistler burst versus the corresponding value observed at the end of this burst. It is seen that in the majority of cases the value of  $T_{\text{PER}}/T_{\text{PAR}}$  is larger at the start of the burst and decreases by the end of the burst (the dots are below the dashed line in Figure 8). This result would be in agreement with the idea that whistler waves worked to isotropize the electron distribution function. Note that magnetospheric whistler waves are believed to be responsible for diffuse aurora via scattering electrons into the loss cone (Kasahara et al., 2018; Ni et al., 2011; Nishimura et al., 2010; Thorne et al., 2010). Panov et al., 2013 have demonstrated that whistler waves at DFs are capable of scattering the electrons with energies up to about 5 keV into the loss cone and that significant part of these electrons is absent at the DFs simultaneously with the presence of diffuse aurora in the conjugate ionosphere. The above facts manifest that generally the system is open to the ionosphere. Hence, the resulting electron distribution function at the DFs is also the result of interplay of a number of processes. Such processes include betatron acceleration, generation of whistler wave aimed at decreasing the perpendicular anisotropy of the electron distribution function, and scattering of electrons by whistlers and other (e.g., electrostatic cyclotron harmonic; Wendel et al., 2019) waves.

Temperature anisotropy is an integral parameter that does not provide the information on the particular energy range and pitch angles of the local electron population capable to contribute to the maximum of growth rate and/or efficiently interact with the quasi-parallel whistler waves. Using the advantage of the high-resolution MMS observations, we calculate the growth rate from 3-D electron velocity distribution functions averaged over 120 ms within each burst of whistler waves from our database. Then, at each time we determine the energies  $W_{\text{res}}$  and pitch angles,  $\alpha_{\text{res}}$ , of the resonant electrons making maximum contribution to the growth rate. We have found that for the majority of whistler bursts from our database,  $W_{\text{res}}$  is  $\sim 1\text{--}5$  keV and the maximum of observation

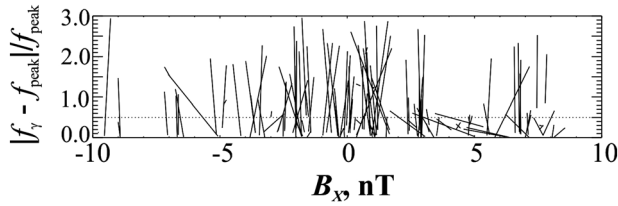


**Figure 9.** Dashed lines display the  $|f_{\text{peak}} - f_{\gamma}|/f_{\text{peak}}$  values versus the  $B_X$  field observed at every 120 ms time bin within each whistler burst from our database (see explanations in the text). The dotted horizontal line marks the level  $|f_{\text{peak}} - f_{\gamma}|/f_{\text{peak}} = 0.5$ .

electrons can be a free energy source for excitation of whistler waves within and around DFs. Here by calculation of the growth rate of quasi-parallel whistler waves we showed that electrons with energies  $\sim 1\text{--}5$  keV are able to interact efficiently with these waves and contribute to their growth rate. This results in modification of the local electron distribution function in this energy range.

In order to trace how  $W_{\text{res}}$  changes in the course of a DF event, in Figure 5f we plot the epoch profile of the median value of  $W_{\text{res}}$ . It is seen that statistically the value of  $W_{\text{res}}$  is higher ( $>3$  keV) at and immediately behind the DF (during  $\sim 15$  s after the start of DF). Behind the DF in the DFB,  $W_{\text{res}}$  decreases and becomes  $\leq 3$  keV.

We found that in quasi-parallel whistler waves from our database, electrons with  $\alpha_{\text{res}} \sim 40\text{--}75^\circ$  and  $100\text{--}135^\circ$  make maximum contribution to their growth rate. Electrons with pitch angles close to  $0^\circ$  or  $180^\circ$  do not contribute to the growth rate. This implies that even in those few whistler bursts, which were associated with  $T_{\text{PER}}/T_{\text{PAR}} < 1$ , the main contribution to the growth rate was made by electrons with large pitch angles.

To check if the source of the observed whistler wave is located near MMS spacecraft, we have compared the observed frequency of the whistler waves ( $f_{\text{peak}}$ ) with the frequencies corresponding to the maximum of growth rate ( $f_{\gamma}$ ) calculated from the local 3-D electron velocity distribution within the wave burst.

To make the comparison, we calculate  $|f_{\text{peak}} - f_{\gamma}|/f_{\text{peak}}$  value for every 120 ms time bin within each burst. In Figure 9 we plot this values versus the value of the  $B_X$  field observed at a given time bin within each burst from our database. Each line in the figure corresponds to the particular whistler burst. We found that within each burst the  $|f_{\text{peak}} - f_{\gamma}|/f_{\text{peak}}$  varies from almost 0 value indicating the proximity of the wave source to the spacecraft and up to a few units. The large  $|f_{\text{peak}} - f_{\gamma}|/f_{\text{peak}}$  values denote that at such moments the local electron velocity distribution is hardly responsible for the generation of the wave with the observed frequency  $f_{\text{peak}}$ . Within the majority of bursts from our database both small ( $<0.5$ ) and large ( $>0.5$ )  $|f_{\text{peak}} - f_{\gamma}|/f_{\text{peak}}$  values are observed. Such diversity observed within one and the same quasi-parallel whistler burst may denote that the spacecraft crossed the magnetic flux tubes mapping into the spatially spread source of the whistler wave. Thus, while the magnetic structure passes by the spacecraft, the latter either approaches the wave source and registers  $|f_{\text{peak}} - f_{\gamma}|/f_{\text{peak}} \sim 0$ , or it moves away from the source and detects larger  $|f_{\text{peak}} - f_{\gamma}|/f_{\text{peak}}$  values (see a cartoon in Figure 10).

We did not find a significant difference between the amplitude of variations of  $|f_{\text{peak}} - f_{\gamma}|/f_{\text{peak}}$  values within the bursts observed near the neutral plane (at  $|B_X| < 5$  nT) and those observed at larger  $|B_X|$ . Regardless of the  $B_X$  location of the spacecraft, at some times within the majority of bursts the observed  $f_{\text{peak}}$  casually was almost equal to the  $f_{\gamma}$ . Thus, at such times the local electron distribution function was able to generate the whistler wave with the observed frequency. We

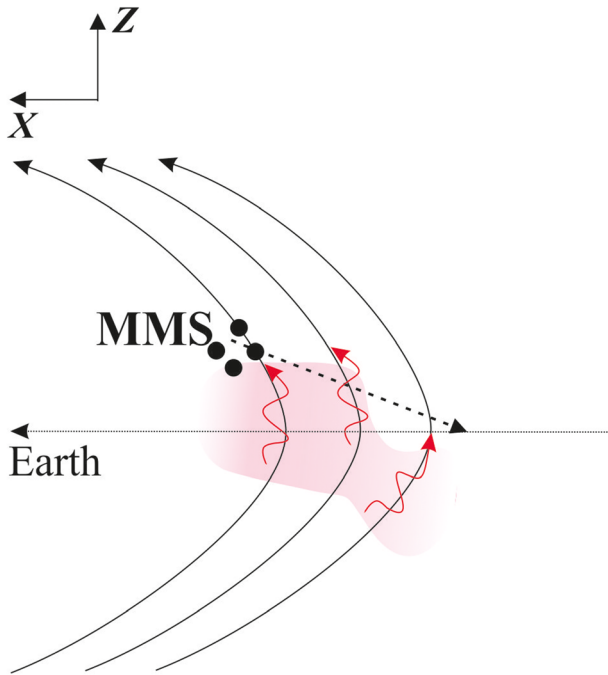


**Figure 10.** A cartoon illustrated a spatially extended source (shaded by pink) of the quasi-parallel whistler waves (shown by red lines) propagating to the spacecraft along the dipolarizing magnetic field lines (shown by black lines). The spacecraft trajectory is displayed by the dashed line.

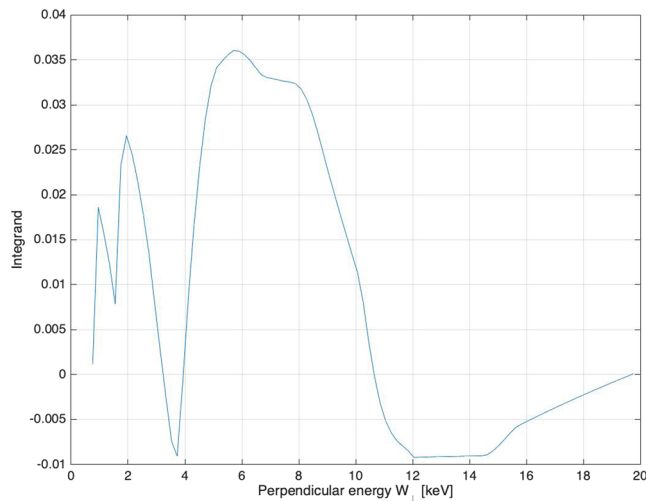


**Figure 11.** The integrand of the Expression 1, which determines the growth rate  $\gamma$ , after transforming the variable of integration from  $s = \sin^2\alpha$  to particle transversal energy  $W_{\perp} = W_{\parallel\text{res}} \tan^2\alpha$  at fixed  $W_{\parallel\text{res}}$ . Calculations correspond to MMS-1 electron flux measurements on 19 June 2017 at 03:57:40 UT, performed for the whistler wave with  $\mathbf{k} \cdot \mathbf{B} < 0$  and  $f = f_{\gamma}$ .

may suggest that in the DF events the source of quasi-parallel whistler waves is not confined near the neutral plane but that it is spatially extended in the PS region (at larger  $|B_{\chi}|$ ). As soon as the perpendicular anisotropy appears in the local electron distribution function it contributes to the positive growth rate of quasi-parallel whistler waves. Such anisotropy can be formed due to the betatron energization of electrons in a growing magnetic field (e.g., Fu et al., 2011; Khotyaintsev et al., 2011).

The primary purpose of comparison between whistler spectra and differential electron fluxes in DFs is to explain the origin of whistler mode wave activity, which we attribute to cyclotron instability of the observed energetic electron distribution. Since this instability is mostly related to electrons with fairly large pitch angles, as the amplitude of electron interaction with parallel propagating whistler mode wave is proportional to particle perpendicular velocity, we do not expect this interaction to lead to electron precipitation in the auroral zone conjugated to DFs. At the same time, the excitation of whistler mode waves by unstable electron distribution is accompanied by energy exchange between particles with different perpendicular velocities through the excited waves and in some cases can lead to energy transfer from lower- to higher-energy particles, which is not forbid-

den in an unstable and, thus, nonequilibrium medium (Shklyar, 2011, 2017). The presence of this process in the situation under discussion is illustrated by Figure 11, which shows the integrand of the integral with respect to  $W_{\perp}$  that determines the contribution to the growth rate  $\gamma$  made by electrons with perpendicular energy  $W_{\perp}$ . It is calculated from the local electron distribution function observed by MMS-1 on 19 June 2017 at 03:57:40 UT (during the Burst I discussed in section 2) by using Equations 1 and 2 and transforming the variable of integration from  $s = \sin^2\alpha$  to  $W_{\perp} = W_{\parallel\text{res}} \tan^2\alpha$  at fixed  $W_{\parallel\text{res}}$ . It is seen that particles with lower  $W_{\perp}$  make positive contribution to  $\gamma$ , which means that these particles lose their energy. On the contrary, the contribution to  $\gamma$  from higher-energy particles is negative, implying that their energy increases. This effect was also observed in the dynamics of fluxes of lower-energy and higher-energy electrons during the wave bursts (see Figures 3f–3j). We should stress that the Expression 1 for the growth rate arises after integration with respect to particle parallel velocity and gyrophase over the resonance region and, thus, only gives an idea about an average variation of resonant particle kinetic energy. The mean square variation cannot be restored from the expression for linear growth rate and requires special consideration. Thus, excitation of whistler mode waves in DFs by unstable electron distribution leads to, probably measurable, increase of electron energy of some fraction of energetic electrons, which was shown by Grigorenko et al., 2016. At the same time, the wave growth implies that larger fraction of particles transforms its free energy to the wave, which constrains the temperature anisotropy of the total electron distribution. We should mention that energy variations of particles are accompanied by their pitch angle variations, which, however, is insignificant for particles close to the loss cone.

## 5. Conclusions

MMS observations in burst mode make it possible for the first time to analyze the anisotropy of electron velocity distributions and calculate the growth rate of quasi-parallel narrowband whistler waves on the time scale of their bursts (approximately a few seconds). The majority of the whistler bursts from our database were associated with perpendicular electron anisotropy  $T_{\text{PER}}/T_{\text{PAR}} > 1$ , and the value of this anisotropy decreases by the end of the burst suggesting the electron scattering by the waves. We have found that electrons with energies  $W_{\text{res}} \sim 1\text{--}5$  keV and pitch angles near  $60^\circ$  and  $120^\circ$  make the major contribution to the growth rate of these waves. The largest  $W_{\text{res}} (> 3$  keV) is observed at the DF and immediately behind it, while in the DFB region the  $W_{\text{res}}$  decrease below 3 keV in the majority of cases.

In the DF events the source of quasi-parallel narrowband whistler waves is likely not confined near the neutral plane but rather has a broader extent into the PS region where the perpendicular anisotropy in the local electron velocity distribution ensures a positive growth rate of whistler waves.



To summarize, we have shown that whistler waves play an important role in self-consistent dynamics of electron velocity distribution function in DFs. Being excited due to cyclotron instability caused by temperature anisotropy of suprathermal electron distribution, these waves serve as a conduit for energy transfer between different parts of electron population, and at the same time, constrain the overall temperature anisotropy of electron distribution.

**Acknowledgments**

We thank the MMS Data Center (<https://lasp.colorado.edu/mms/sdc/public/>) and CLWEB (<http://clweb.irap.omp.eu/>) from which the data used in this paper were obtained. The work of E. E. G. and A. Yu. M. was supported by Russian Science Foundation (Grant 18-47-05001). D. R. S. acknowledges support from RFBR Grant 19-02-00179. E. V. P. acknowledges support from the Austrian Science Fund (FWF): I 3506-N27. The French involvement in the FPI and SCM instruments is supported by CNES and CNRS.

**References**

Akilov, G. P., & Kantorovich, L. V. (1982). *Functional analysis* (2nd ed.). Elsevier, Oxford, England: Pergamon Press.

Angelopoulos, V., Baumjohann, W., Kennel, C. F., Coroniti, F. V., Kivelson, M. G., Pellat, R., et al. (1992). Bursty bulk flows in the inner central plasma sheet. *Journal of Geophysical Research*, *97*(A4), 4027–4039. <https://doi.org/10.1029/91JA02701>

Balikhin, M. A., Runov, A., Walker, S. N., Gedalin, M., Dandouras, I., Hobara, Y., & Fazakerley, A. (2014). On the fine structure of dipolarization fronts. *Journal of Geophysical Research: Space Physics*, *119*, 6367–6385. <https://doi.org/10.1002/2014JA019908>

Birn, J., Merkin, V. G., Sitnov, M. I., & Otto, A. (2018). MHD stability of magnetotail configurations with a Bz hump. *Journal of Geophysical Research: Space Physics*, *123*, 3477–3492. <https://doi.org/10.1029/2018JA025290>

Birn, J., Runov, A., & Hesse, M. (2014). Energetic electrons in dipolarization events: Spatial properties and anisotropy. *Journal of Geophysical Research: Space Physics*, *119*, 3604–3616. <https://doi.org/10.1002/2013JA019738>

Breuillard, H., le Contel, O., Retino, A., Chasapis, A., Chust, T., Mirioni, L., et al. (2016). Multi spacecraft analysis of dipolarization fronts and associated whistler wave emissions using MMS data. *Geophysical Research Letters*, *43*, 7279–7286. <https://doi.org/10.1002/2016GL069188>

Burch, J. L., Moore, T. E., Torbert, R. B., & Giles, B. L. (2016). Magnetospheric Multiscale overview and science objectives. *Space Science Reviews*, *199*(1-4), 5–21. <https://doi.org/10.1007/s11214-015-0164-9>

Cornilleau-Wehrlin, N., Solomon, J., Korth, A., & Kremser, G. (1985). Experimental study of the relationship between energetic electrons and ELF waves observed on board GEOS: A support to quasi-linear theory. *Journal of Geophysical Research*, *90*(A5), 4141–4154. <https://doi.org/10.1029/JA090iA05p04141>

Fu, H., Grigorenko, E. E., Gabrielse, C., Liu, C., Lu, S., Hwang, K. J., et al. (2020). Magnetotail dipolarization fronts and particle acceleration: A review. *Science China Earth Sciences*, *63*(2), 235–256. <https://doi.org/10.1007/s11430-019-9551-y>

Fu, H. S., Khotyaintsev, Y. V., André, M., & Vaivads, A. (2011). Fermi and betatron acceleration of suprathermal electrons behind dipolarization fronts. *Geophysical Research Letters*, *38*, L16104. <https://doi.org/10.1029/2011GL048528>

Fu, H. S., Khotyaintsev, Y. V., Vaivads, A., Andre, M., Sergeev, V., Huang, S., et al. (2012). Pitch angle distribution of suprathermal electrons behind dipolarization fronts. A statistical overview. *Journal of Geophysical Research*, *117*, A12221. <https://doi.org/10.1029/2012JA018141>

Gabrielse, C., Harris, C., Angelopoulos, V., Artemyev, A., & Runov, A. (2016). The role of localized inductive electric fields in electron injections around dipolarizing flux bundles. *Journal of Geophysical Research: Space Physics*, *121*, 9560–9585. <https://doi.org/10.1002/2016JA023061>

Grigorenko, E. E., Kronberg, E. A., Daly, P. W., Ganushkina, N. Y., Lavraud, B., & Sauvaud, J.-A., & Zelenyi, L. M. (2016). Origin of low proton-to-electron temperature ratio in the Earth's plasma sheet. *Journal of Geophysical Research: Space Physics*, *121*, 9985–10,004. <https://doi.org/10.1002/2016JA022874>

Gurnett, D. A., Frank, L. A., & Lepping, R. P. (1976). Plasma waves in the distant magnetotail. *Journal of Geophysical Research*, *81*(34), 6059–6071. <https://doi.org/10.1029/JA081i034p06059>

Huang, S. Y., Zhou, M., Deng, X. H., Yuan, Z. G., Pang, Y., Wei, Q., et al. (2012). Kinetic structure and wave properties associated with sharp dipolarization front observed by Cluster. *Annales de Geophysique*, *30*(1), 97–107. <https://doi.org/10.5194/angeo-30-97-2012>

Kasahara, S., Miyoshi, Y., Yokota, S., Mitani, T., Kasahara, Y., Matsuda, S., et al. (2018). Pulsating aurora from electron scattering by chorus waves. *Nature*, *554*(7692), 337–340. <https://doi.org/10.1038/nature25505>

Khotyaintsev, Y. V., Cully, C. M., Vaivads, A., André, M., & Owen, C. J. (2011). Plasma jet braking: Energy dissipation and nonadiabatic electrons. *Physical Review Letters*, *106*(16), 165001. <https://doi.org/10.1103/PhysRevLett.106.165001>

Le Contel, O., Leroy, P., Roux, A., Coillot, C., Alison, D., Bouabdellah, A., et al. (2016). The search-coil magnetometer for MMS. *Space Science Reviews*, *199*(1-4), 257–282. <https://doi.org/10.1007/s11214-014-0096-9>

Le Contel, O., Roux, A., Jacquey, C., Robert, P., Berthomier, M., Chust, T., et al. (2009). Quasi-parallel whistler mode waves observed by THEMIS during near-Earth dipolarizations. *Annales de Geophysique*, *27*(6), 2259–2275. <https://doi.org/10.5194/angeo-27-2259-2009>

Liang, J., Ni, B., Cully, C. M., Donovan, E. F., Thorne, R. M., & Angelopoulos, V. (2012). Electromagnetic ELF wave intensification with fast earthward flows in mid-tail plasma sheet. *Annales de Geophysique*, *30*(3), 467–488. <https://doi.org/10.5194/angeo-30-467-2012>

Liu, C. M., & Fu, H. S. (2019). Anchor point of electron acceleration around dipolarization fronts in space plasmas. *Astrophysical Journal Letters*, *873*(1), L2. <https://doi.org/10.3847/2041-8213/ab06cb>

Liu, J., Angelopoulos, V., Runov, A., & Zhou, X.-Z. (2013). On the current sheets surrounding dipolarizing flux bundles in the magnetotail. The case of wedgelets. *Journal of Geophysical Research*, *118*, 2000–2020. <https://doi.org/10.1002/jgra.50092>

Liu, J., Angelopoulos, V., Runov, A., & Zhou, X.-Z. (2014). Magnetic flux transport by dipolarizing flux bundles. *Journal of Geophysical Research: Space Physics*, *119*, 909–926. <https://doi.org/10.1002/2013JA019395>

Liu, C. M., Fu, H. S., Cao, J. B., Xu, Y., Yu, Y. Q., Kronberg, E. A., & Daly, P. W. (2017). Rapid pitch angle evolution of suprathermal electrons behind dipolarization fronts. *Geophysical Research Letters*, *44*, 10,116–10,124. <https://doi.org/10.1002/2017GL075007>

Merkin, V. G., Panov, E. V., Sorathia, K., & Ukhorskiy, A. Y. (2019). Contribution of bursty bulk flows to the global dipolarization of the magnetotail during an isolated substorm. *Journal of Geophysical Research: Space Physics*, *124*, 8647–8668. <https://doi.org/10.1029/2019JA026872>

Merkin, V. G., & Sitnov, M. I. (2016). Stability of magnetotail equilibria with a tailward Bz gradient. *Journal of Geophysical Research*, *121*, 9411–9426. <https://doi.org/10.1002/2016JA023005>

Nakamura, R., Baumjohann, W., Klecker, B., Bogdanova, Y., Balogh, A., Rème, H., et al. (2002). Motion of the dipolarization front during a flow burst event observed by Cluster. *Geophysical Research Letters*, *29*(20), 1942. <https://doi.org/10.1029/2002GL015763>

Ni, B., Thorne, R. M., Meredith, N. P., Shprits, Y. Y., & Horne, R. B. (2011). Diffuse auroral scattering by whistler mode chorus waves: Dependence on wave normal angle distribution. *Journal of Geophysical Research*, *116*, A10207. <https://doi.org/10.1029/2011JA016517>

- Nishimura, Y., Bortnik, J., Li, W., Thorne, R. M., Lyons, L. R., Angelopoulos, V., et al. (2010). Identifying the driver of pulsating aurora. *Science*, 330. <https://doi.org/10.1126/science.1193186>
- Panov, E. V., Artemyev, A. V., Baumjohann, W., Nakamura, R., & Angelopoulos, V. (2013). Transient electron precipitation during oscillatory BBF braking: THEMIS observations and theoretical estimates. *Journal of Geophysical Research: Space Physics*, 118, 3065–3076. <https://doi.org/10.1002/jgra.50203>
- Panov, E. V., Baumjohann, W., Nakamura, R., Pritchett, P. L., Weygand, J. M., & Kubyskhina, M. V. (2019). Ionospheric footprints of detached magnetotail interchange heads. *Geophysical Research Letters*, 46, 7237–7247. <https://doi.org/10.1029/2019GL083070>
- Panov, E. V., Lu, S., & Pritchett, P. L. (2020). Understanding spacecraft trajectories through detached magnetotail interchange heads. *Journal of Geophysical Research: Space Physics*, 125, e2020JA027930. <https://doi.org/10.1029/2020JA027930>
- Pollock, C., Moore, T., Jacques, A., Burch, J., Gliese, U., Saito, Y., et al. (2016). Fast Plasma Investigation for Magnetospheric Multiscale. *Space Science Reviews*, 199(1-4), 331–406. <https://doi.org/10.1007/s11214-016-0245-4>
- Pritchett, P. L. (2015). Instability of current sheets with a localized accumulation of magnetic flux. *Physics of Plasmas*, 22(6). <https://doi.org/10.1063/1.4921666>
- Pritchett, P. L., & Coroniti, F. V. (2011). Plasma sheet disruption by interchange-generated flow intrusions. *Geophysical Research Letters*, 38, L10102. <https://doi.org/10.1029/2011GL047527>
- Pritchett, P. L., Coroniti, F. V., & Nishimura, Y. (2014). The kinetic ballooning/interchange instability as a source of dipolarization fronts and auroral streamers. *Journal of Geophysical Research: Space Physics*, 119, 4723–4739. <https://doi.org/10.1002/2014JA019890>
- Runov, A., Angelopoulos, V., Gabrielse, C., Zhou, X.-Z., Turner, D., & Plaschke, F. (2013). Electron fluxes and pitch-angle distributions at dipolarization fronts: THEMIS multipoint observations. *Journal of Geophysical Research: Space Physics*, 118, 744–755. <https://doi.org/10.1002/jgra.50121>
- Runov, A., Angelopoulos, V., Sitnov, M. I., Sergeev, V. A., Bonnell, J., McFadden, J. P., et al. (2009). THEMIS observations of an earthward propagating dipolarization front. *Geophysical Research Letters*, 36, L14106. <https://doi.org/10.1029/2009GL038980>
- Runov, A., Angelopoulos, V., Zhou, X.-Z., Zhang, X.-J., Li, S., Plaschke, F., & Bonnell, J. (2011). A THEMIS multicase study of dipolarization fronts in the magnetotail plasma sheet. *Journal of Geophysical Research*, 116, A05216. <https://doi.org/10.1029/2010JA016316>
- Russell, C. T., Anderson, B. J., Baumjohann, W., Bromund, K. R., Dearborn, D., Fischer, D., et al. (2016). The Magnetospheric Multiscale magnetometers. *Space Science Reviews*, 199(1-4), 189–256. <https://doi.org/10.1007/s11214-014-0057-3>
- Sagdeev, R. Z., & Shafranov, V. D. (1961). On the instability of a plasma with anisotropic distribution of velocities in a magnetic field. *Soviet Physics - JETP*, 12(1), 130–132.
- Schmid, D., Nakamura, R., Plaschke, F., Volwerk, M., & Baumjohann, W. (2015). Two states of magnetotail dipolarization fronts: A statistical study. *Journal of Geophysical Research: Space Physics*, 120, 1096–1108. <https://doi.org/10.1002/2014JA020380>
- Sergeev, V. A., Angelopoulos, V., Apatenkov, S., Bonnell, J., Ergun, R., Nakamura, R., et al. (2009). Kinetic structure of the sharp injection/dipolarization front in the flow-braking region. *Geophysical Research Letters*, 36, L21105. <https://doi.org/10.1029/2009GL040658>
- Sergeev, V. A., Angelopoulos, V., & Nakamura, R. (2012). Recent advances in understanding substorm dynamics. *Geophysical Research Letters*, 39, L05101. <https://doi.org/10.1029/2012GL050859>
- Shklyar, D., & Matsumoto, H. (2009). Oblique whistler-mode waves in the inhomogeneous magnetospheric plasma: Resonant interactions with energetic charged particles. *Surveys in Geophysics*, 30(2), 55–104. <https://doi.org/10.1007/s10712-009-9061-7>
- Shklyar, D. R. (2011). Wave-particle interactions in marginally unstable plasma as a means of energy transfer between energetic particle populations. *Physics Letters*, 375(14), 1583–1587. <https://doi.org/10.1016/j.physleta.2011.02.067>
- Shklyar, D. R. (2017). Energy transfer from lower energy to higher-energy electrons mediated by whistler waves in the radiation belts. *Journal of Geophysical Research: Space Physics*, 122, 640–655. <https://doi.org/10.1002/2016JA023263>
- Shklyar, D. R., Titovaa, E. E., Manninen, J., & Romantsova, T. V. (2020). Whistler growth rates in the magnetosphere according to measurements of energetic electron fluxes on the Van Allen Probe A satellite. *Geomagnetism and Aeronomy*, 60(1), 46–57. <https://doi.org/10.1134/S0016793220010132>
- Sitnov, M. I., Merkin, V. G., Pritchett, P. L., & Swisdak, M. (2017). Distinctive features of internally driven magnetotail reconnection. *Geophysical Research Letters*, 44, 3028–3037. <https://doi.org/10.1002/2017GL072784>
- Sitnov, M. I., Swisdak, M., & Divin, A. V. (2009). Dipolarization fronts as a signature of transient reconnection in the magnetotail. *Journal of Geophysical Research*, 114, A04202. <https://doi.org/10.1029/2008JA013980>
- Tenerani, A., Le Contel, O., Califano, F., Robert, P., Fontaine, D., Cornilleau-Wehrin, N., & Sauvaud, J.-A. (2013). Cluster observations of whistler waves correlated with ion-scale magnetic structures during the 17 August 2003 substorm event. *Journal of Geophysical Research: Space Physics*, 118, 6072–6089. <https://doi.org/10.1002/jgra.50562>
- Thorne, R. M., Ni, B., Tao, X., Horne, R. B., & Meredith, N. P. (2010). Scattering by chorus waves as the dominant cause of diffuse aurora precipitation. *Nature*, 467(7318), 943–946. <https://doi.org/10.1038/nature09467>
- Trakhtengerts, V. Y., & Rycroft, M. J. (2008). *Whistler and Alfvén mode cyclotron masers in space*. Cambridge, UK: Cambridge University Press.
- Viberg, H., Khotyaintsev, Y. V., Vaivads, A., André, M., Fu, H. S., & Cornilleau-Wehrin, N. (2014). Whistler mode waves at magnetotail dipolarization fronts. *Journal of Geophysical Research: Space Physics*, 119, 2605–2611. <https://doi.org/10.1002/2014JA019892>
- Wendel, D. E., Khazanov, G. V., Tripathi, A. K., Singhal, R. P., & Zesta, E. (2019). Source of the bursty bulk flow diffuse aurora: Electrostatic cyclotron harmonic and whistler waves in the coupling of bursty bulk flows to auroral precipitation. *Journal of Geophysical Research: Space Physics*, 124, 6669–6690. <https://doi.org/10.1029/2019JA026606>
- Wiltberger, M., Merkin, V., Lyon, J., & Ohtani, S. (2015). High-resolution global magnetohydrodynamic simulation of bursty bulk flows. *Journal of Geophysical Research: Space Physics*, 120, 4555–4566. <https://doi.org/10.1002/2015JA021080>
- Wu, M. Y., Lu, Q. M., Volwerk, M., Vörös, Z., Zhang, T. L., Shan, L. C., & Huang, C. (2013). A statistical study of electron acceleration behind the dipolarization fronts in the magnetotail. *Journal of Geophysical Research: Space Physics*, 118, 4804–4810. <https://doi.org/10.1002/jgra.50456>
- Wu, P., Fritz, T. A., Larvaud, B., & Lucek, E. (2006). Substorm associated magnetotail energetic electrons pitch-angle evolutions and flow reversals: Cluster observation. *Geophysical Research Letters*, 33, L17101. <https://doi.org/10.1029/2006GL026595>
- Yao, S. T., Shi, Q. Q., Yao, Z. H., Li, J. X., Yue, C., Tao, X., et al. (2019). Waves in kinetic-scale magnetic dips: MMS observations in the Magnetosheath. *Geophysical Research Letters*, 46, 523–533. <https://doi.org/10.1029/2018GL080696>
- Zhang, X., Angelopoulos, V., Artemyev, A. V., & Liu, J. (2018). Whistler and electron firehose instability control of electron distributions in and around dipolarizing flux bundles. *Geophysical Research Letters*, 45, 9380–9389. <https://doi.org/10.1029/2018GL079613>

- Zhang, X., Angelopoulos, V., Artemyev, A. V., & Liu, J. (2019). Energy transport by whistler waves around dipolarizing flux bundles. *Geophysical Research Letters*, *46*, 11,718–11,727. <https://doi.org/10.1029/2019GL084226>
- Zhang, X.-J., & Angelopoulos, V. (2014). On the relationship of electrostatic cyclotron harmonic emissions with electron injections and dipolarization fronts. *Journal of Geophysical Research: Space Physics*, *119*, 2536–2549. <https://doi.org/10.1002/2013JA019540>
- Zhang, Y., Matsumoto, H., & Kojima, H. (1999). Whistler mode waves in the magnetotail. *Journal of Geophysical Research*, *104*, 28,633–28,644. <https://doi.org/10.1029/1999JA900301>
- Zhao, M. J., Fu, H. S., Liu, C. M., Chen, Z. Z., Xu, Y., Giles, B. L., & Burch, J. L. (2019). Energy range of electron rolling pin distribution behind dipolarization front. *Geophysical Research Letters*, *46*, 2390–2398. <https://doi.org/10.1029/2019GL082100>